Progress in Additive Manufacturing
https://doi.org/10.1007/s40964-024-00607-y

FULL RESEARCH ARTICLE

Characterization of flexural fatigue behaviour of additively manufactured (PBF–LB) gyroid structures

Garvin Schultheiß[1] · **Burkhard Heine**[1] · **Markus Merkel**[1]

Received: 13 October 2023 / Accepted: 19 March 2024

Abstract
Additive manufacturing (AM) holds remarkable potential for producing cellular materials with intricate structures and tailored mechanical properties. The study investigates the flexural fatigue behaviour of additively manufactured triply periodic minimal surface (TPMS) gyroid structures using laser powder bed fusion (PBF–LB) technique. The fatigue properties, especially the bending fatigue properties, of additively manufactured cellular structures are not well understood to date. The research aims to enhance understanding of bending fatigue in complex cellular geometries and assess the suitability of rotating bending tests. The PBF–LB process parameters were modified to study their impact on the specimen's fatigue properties. The modified parameters led to increased surface roughness but significantly improved fatigue behaviour. This enhancement is attributed to a reduction in build defects, namely pores and finer grain size in thin-walled structures. The study also includes analysis of microstructure, hardness, surface roughness, and porosity of the specimens. The results indicate that optimizing process parameters for thin walled cellular structures can lead to substantial improvements in fatigue strength, at the expense of increased surface roughness. This finding offers practical insights for applications in which a rough surface finish may not be critical or even intentionally desired by the application. The research contributes to the understanding of additive manufacturing, cellular structures, and material testing, with potential implications for materials science and engineering applications.

Keywords Triply Periodic Minimal Surfaces (TPMS) · Rotating Bending test · Cellular Geometries · Selective Laser Melting (SLM) · Laser Powder Bed Fusion (L-PBF) · Fatigue testing

1 Introduction

Additive manufacturing (AM) has ushered in transformative prospects for material science and engineering. Within this evolving landscape, laser powder bed fusion (PBF–LB) has emerged as a pivotal technique, offering unique geometric degrees of freedom that cater to intricate structures, particularly thin-walled cellular geometries. This has significant implications for lightweight construction, heat exchangers, energy absorbers, and similar applications [1].

✉ Garvin Schultheiß
garvin.schultheiss@hs-aalen.de

Burkhard Heine
burkhard.heine@hs-aalen.de

Markus Merkel
markus.merkel@hs-aalen.de

[1] Institute for Virtual Product Development, Aalen University, Beethovenstraße 1, 73430 Aalen, Germany

AM allows designs to transcend the confines of traditional manufacturing limitations. Furthermore, its resource-efficiency, where only necessary material is utilized and unused powder is recyclable, aligns with sustainable practices. A noteworthy advantage of additive manufacturing lies in its capacity to modulate mechanical properties through the implementation of cellular geometries. The ability to tweak attributes such as relative density, unit cell shape, process parameters, surface roughness, and material choice enables tailored material behaviour within material-specific constraints [2].

The connection between relative density and strength properties in cellular structures, initially established by Ashby et al. [3], has found broad experimental validation among the research community [4]. This highlights the relative density as one of the most important parameters for tailoring the mechanical properties of additively manufactured cellular materials.

Published online: 10 April 2024

Triply periodic minimal surface (TPMS) structures, characterized by their continuous periodic nature and superior strength-to-weight ratios compared to other unit cell shapes [5], have demonstrated utility in diverse applications such as lightweight construction [6, 7], heat exchangers [8], energy absorbers [9] and biomedical implants [10, 11].

In materials testing, surface roughness is recognized as a critical factor influencing the fatigue strength of components [12]. Given the scan parameters used, the PBF–LB process inherently introduces elevated surface roughness, and this aspect becomes particularly pronounced in the fabrication of thin-walled components. Frequently, a compromise between surface roughness and the density of the component's solid volume becomes necessary [13]. Although the substantial surface roughness of as-built PBF–LB samples is acknowledged to impact fatigue behaviour, attempts to enhance this through surface polishing, have yielded inconsistent results [14–16]. This points to internal defects and microstructural properties as principal determinants of fatigue behaviour of PBF–LB parts [17].

Amid this backdrop, the study of as-built fatigue properties of thin walled cellular structures, especially bending fatigue, warrants attention. Current research on the fatigue properties of cellular materials remain limited, opening avenues for comprehensive investigation [4, 18]. To characterise the mechanical properties of cellular materials, compression tests are usually employed. Two primary factors support the preference for compressive testing on lattice structures: the prevalence of compressive load cases and the straightforward test setup. Compressive testing involves subjecting a structure to compression between two plates until collapse, with the resultant force being measured. There are limited studies on the fatigue properties of additively manufactured lattice structures, and these primarily focus on compression–compression behaviour, resulting in significant neglect of the bending load case [4, 18]. The limited studies on the flexural fatigue properties of additively manufactured cellular structures were conducted using 3-point flexural tests, which necessitated encasing the test structure in a sandwich-style arrangement to ensure the structural integrity of the delicate filigree structure was maintained [19].

This research paper aims to characterize the flexural fatigue properties of as-built radially arranged triply periodic minimal surface gyroid structures manufactured via PBF–LB. Utilizing the rotating bending test, the study seeks to enhance comprehension of bending fatigue behaviour in intricate cellular geometries and to investigate the suitability of the method. To achieve this, two sets of samples with varying PBF–LB parameters were designed, manufactured using AlSi10Mg, and subjected to rotating bending tests, surface roughness tests, optical density analysis as well as SEM and light microstructure examinations. With a practical focus on as-built components, the investigation refrains from surface finishing or thermal post-treatment as the practical aspect of reducing surface roughness to economize the production costs of series components is typically disregarded. In line with this, our primary intention was to subject specimens to testing with practical, as-built surface characteristics. We expect that the component's porosity, relative density, and surface roughness will have an influence on its fatigue properties.

Anticipated outcomes extend beyond the study's scope, potentially informing broader materials science and engineering applications. Insights derived may be transferable to other materials, such as stainless steels for heat exchangers or titanium alloys for biomedical implants. This pursuit aims to explore new aspects of additive manufacturing, cellular structures and material testing, contributing to the advancement of technical practice and knowledge.

2 Materials and methods

2.1 Specimen design

Unit cells can be arranged in various configurations, leading to distinct geometries. In Fig. 1b, a non-conformal homogeneous cell arrangement is presented within a cylindrical block with a hole along its rotational axis. The cylinder's boundaries are independent of cell properties, resulting in an uneven shell surface. In contrast, Fig. 1c illustrates radially conformal unit cells that adapt to the cylindrical contour, varying in size across the cross section to maintain conformity. As a result, the relative density varies across the specimen's cross section. The specimens in this study feature an arrangement of radially conformal unit cells around a 1 mm diameter recess along the rotation axis.

The outer contour of the specimen geometry follows the specifications from DIN 503113:2018–12 [20] with the central portion being replaced by a cellular structure. This cellular structure gradually increases its wall thickness and diameter toward the 12.2 mm shafts, as shown in Fig. 2a. The selected cell geometry is the “Gyroid Schoen” form, initially described by Alan Schoen in 1970 [21], depicted in Fig. 1a.

The cells are arranged radially, as illustrated in Fig. 1c, causing the cell size and, consequently, the specimen's relative density to vary across the diameter. In the outermost row of the central part, samples consist of 4 mm × 4 mm unit cells with a 0.5 mm wall thickness. The wall thickness remains unaffected by the conformal arrangement, while the unit cell size diminishes toward the rotation axis of the specimen to facilitate conformity, resulting in a calculated relative porosity of 70% for the central part of the specimen under investigation. Additionally, the samples incorporate a 1 mm diameter recess along the rotation axis to ensure

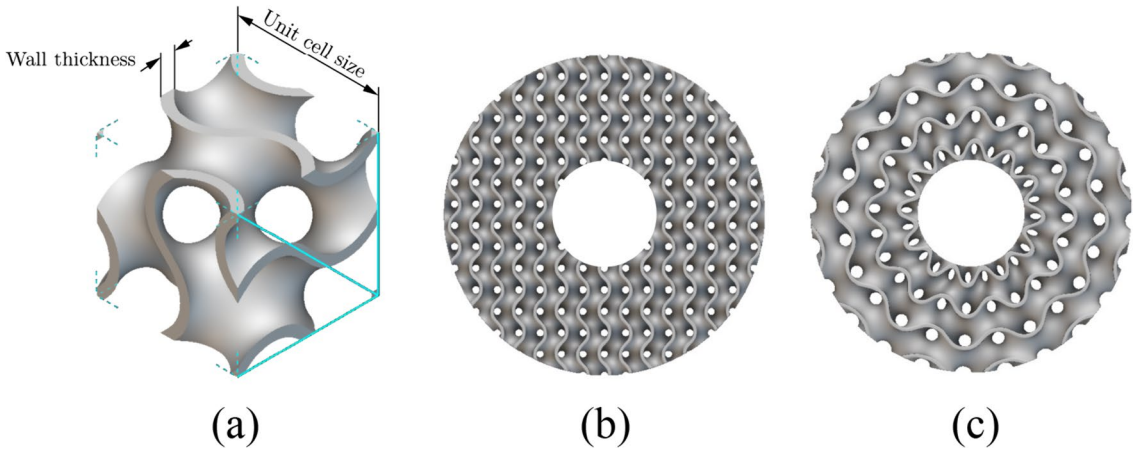

Fig. 1 **a** Gyroid Schoen unit cell, and **b** non-conformal vs. **c** radially conformal Gyroid arrangement

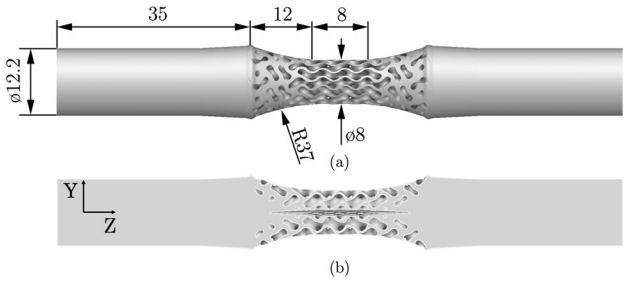

Fig. 2 **a** Specimen geometry and exact dimensions, **b** YZ section of the specimen geometry showing the central cavity

effective powder removal, as shown in the cross section in Fig. 2b. For precise geometrical specifications, refer to Fig. 2a.

The complex features of the sample geometry were calculated using field-driven design within the software nTopology (nTop Inc., USA). The continuous augmentation of the wall thickness and the diameter aims to avoid sudden jumps in Young's modulus and the section modulus within the transition zone of the structure and shaft, allowing a targeted investigation of the cylindrical 8 mm × 8 mm cell structure in the gage length.

2.2 PBF–LB sample fabrication

An SLM 280 HL PBF–LB system (SLM Solutions Group AG, Germany) was employed for fabricating the samples in this research. All samples were manufactured with a layer height of 30 µm under an argon inert gas atmosphere, using AlSi10Mg powder sourced from SLM Solutions Group AG, Germany with a relative humidity of less than 5%.

A total of 50 specimens were fabricated, with 25 printed using the standard parameters (Std.Par) for AlSi10Mg provided by SLM-Solutions AG, and 25 employing a modified parameter set (Mod.Par). The relevant parameters for each set are detailed in Table 1. Within the modified parameter set, changes were made to the beam compensation, the border distance as well as the scanning speed, the laser power and the build platform temperature. The beam compensation parameter governs the distance between the centre of the contour beam and the geometry's border contour. The reduction of this parameter in combination with the

Table 1 PBF–LB Process parameters for the manufacture of the rotating bending specimens divided into the Standard parameters (Std.Par) and the modified Parameters (Mod.Par)

		Hatch		Borders	
		Std. Par	Mod.Par	Std.Par	Mod.Par
Scan speed	[mm/s]	1335	1400	730	900
Laser power	[W]	370	350	300	170
Hatch distance	[mm]	0.17	0.12		
Number of borders				1	2
Border distance	[mm]			0.2	0.05
Beam compensation	[mm]			0.164	0.06
Vol. energy density (VED)	[J/mm^3]	54.34	69.44		
Track energy density (TED)	[J/mm]	0.28	0.25	0.41	0.19
Build plate temp	[°C]	150	200	150	200

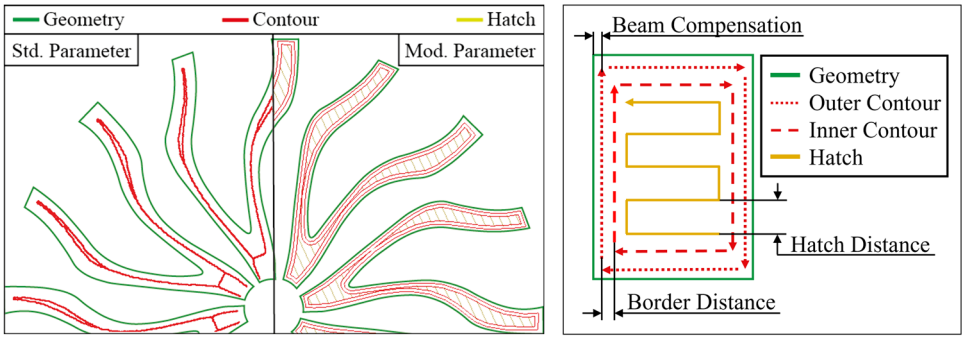

Fig. 3 (left) Resulting scanning vectors from the parameter modification and (right) definition of the relevant scanning parameters in Table 1

Table 2 Porosity of the two test specimens determined optically on the basis of the micrographs

	Optical density [%]	
	Standard parameters	Modified parameters
Shafts	99.87	99.90
Gyroid structure	99.17	99.90

A differentiation is made between the total porosity of the microsection and the porosity only in the thin walled gyroid structure

reduced border distance, leads to two contour scan lines of the delicate 0.5 mm walls. This contrasts with the standard parameters, which utilize only one contour scan. This distinction is graphically depicted in Fig. 3, showcasing the calculated laser trajectories of both parameter sets on the same layer within the specimen's centre. The geometry outline is given in green, contour parameters are highlighted in red, while hatch parameters are represented in yellow. Notably, the modified parameter set accommodates two contour scans and a hatch on the slender wall geometry, whereas the standard parameters use a single contour scan to meet the geometry requirements. Both the standard parameter and the modified parameter scan from the inside to the outside. This means the following sequence: first the hatch, if present, is exposed, then the inner contour and finally the outer contour.

To manage energy input while executing multiple scans, the laser power of the contours was nearly halved, and the scan speed was notably increased in the modified parameter set. Despite this adjustment, the total energy input of the modified parameters was still increased on this specific geometry, due to the execution of two contours plus a hatch instead of a single contour. Achieving optimal parameters for thin-walled structures requires an extensive parameter study which falls out of the scope of this work (Table 2).

All samples were manufactured without incidents and exhibit no visual defects. It is noticeable that the surface of the specimens manufactured with the modified parameters exhibits a significantly rougher texture, but in return, they appear to have a higher level of detail resolution of the filigree walls, as can be seen in Fig. 4. Due to the complex thermal conditions during manufacturing, which can result in residual stresses within the fabricated component, there are geometric inaccuracies related to the concentricity of the shafts. To address this, the concentricity of the shafts was ensured through lathe machining, with both shafts being turned down to a diameter of 12.0 mm.

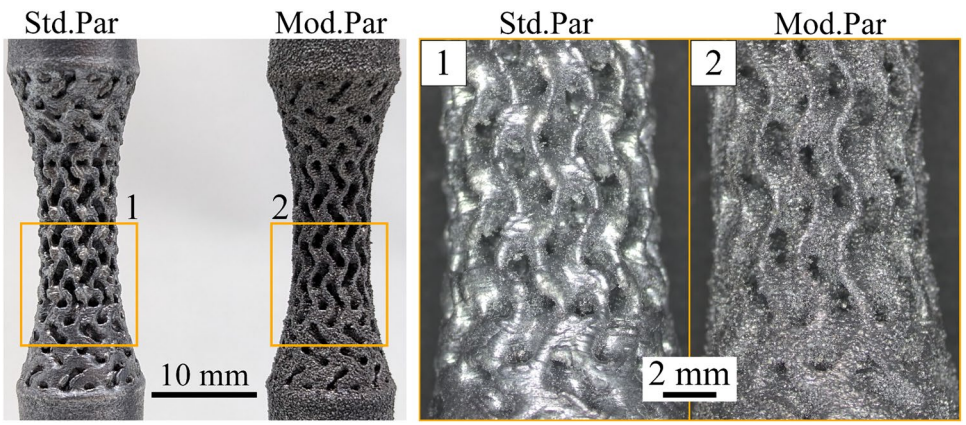

Fig. 4 (left) Resulting specimens from the respective parameters (right) enlargement of the indicated section

2.3 Experimental details

The rotating bending tests were conducted using a Italsigma 2 TM831 rotating bending machine (Italsigma s.r.l, Italy) with a stress ratio, R = − 1 and 20 Hz rotation frequency. Due to the intricate cell geometries present in the test specimens, employing the conventional method of calculating bending stress using data from attached strain gauges and theoretical bending stresses proves challenging. Consequently, an empirical approach is adopted, utilizing the deflection *"f"* of the specimen's centre as a measure rather than the bending stress. The adaptation of the rotating bending test was driven by practical considerations due to the complexity of the specimen's geometry and allows for a comparative analysis of the porous specimens investigated in this work. The principle of displacement measurement is illustrated in Fig. 5. This approach enables the determination of cycle count based on the sample's deflection. The deflection is measured using a dial gauge (Hahn & Kolb, Germany) positioned from the top at the specimen's centre. Different weights were applied, resulting in deflections ranging from 0.1 mm to 1 mm. Each deflection was tested five times for each parameter set, yielding two independent Woehler curves. The examined deflection horizons cover 0.1 mm, 0.15 mm, 0.25 mm, 0.5 mm, and 1 mm. To achieve the respective deflections, identical weights were applied to both set of specimens, indicating similar stiffness.

One sample from both the standard parameter set and the modified parameter set was cut in the centre, embedded in epoxy resin, and polished to a mirror-like finish, after which they were treated with Dix & Keller reagent. SEM images of the microstructure of the thin walls in the centre of the specimen were taken using a Zeiss Sigma 300VP (Carl Zeiss AG, Germany) at an acceleration voltage of 5 kV. Light microscope images were taken with a Zeiss Axioscope 7 (Carl Zeiss AG, Germany).

For each set of parameters, 5 roughness measurements were taken before turning at 3 randomly selected locations along the shafts orthogonal to the build direction using a Zygo NewView 8300 (Zygo Corporation, USA) white-light interferometer.

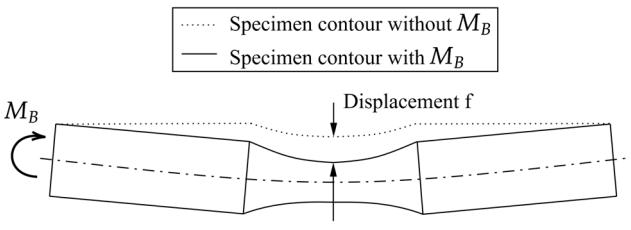

Fig. 5 Illustration of the specimen displacement f measured for the rotating bending tests

Optical porosity analysis was conducted using ImageJ software [22] with microscopic images capturing the entire cross section of a sample from each parameter set.

Exploratory hardness tests were conducted on two fractured specimens from different parameter sets. Vickers HV0.3 microhardness tests were performed following ISO 6507 [21] guidelines on two cross sections using an Emcotest Durascan (Emco GmbH, Austria) with a test force of 3 N and a dwell time of 10 s at each measuring point. Along the rotational axis of each sample geometry, 20 measuring heights were selected, spaced 5 mm apart from one another (refer to Fig. 8). Multiple measurements per height were taken near the fracture point, and a mean value with standard deviation was calculated.

3 Results and discussion

3.1 Surface roughness

The arithmetic surface roughness of the samples manufactured with the modified parameters is noticeably worse, with an Ra value of 28.4 ± 12.2 µm, compared to the samples with the standard parameters, which exhibit a surface roughness of 3.9 ± 1.6 µm. Also noteworthy is the large standard deviation in the modified parameter samples, indicating significant irregularities on the surface. These irregularities, visible in the white-light interferometry images in Fig. 6, appear to result from powder particles adhering to the specimen's surface.

These results are in line with the detailed studies conducted by Poncelet et al. [13], who examined various scan strategies and offsets on 0.6 mm AlSi10Mg walls and ultra-thin walls consisting of two scan lines, covering parameters similar to those presented in this study. The high surface roughness in the modified parameter samples can thus be attributed to significant protuberances formed by outward-flowing melt pools when the geometry's hatch is exposed first. The already solidified hatch disrupts the contour tracks and pushes them outward toward the unmelted powder [13], which can then partially sinter to the specimens surface. The thin walls of the standard parameter samples in the present work are exposed with a single contour scan, while the modified parameter samples are exposed from the inside out with a small hatch and two subsequent contour scans each. Poncelet et al. [13] report that the phenomenon did not occur in samples that exposed the outer contour first, suggesting that the resulting surface roughness of the modified parameters could be improved by swapping the scan order of the contours.

High surface roughness in AM parts is not necessarily linked to poor fatigue behaviour [14, 23]. Partially melted powder particles, spatters, and powder particles stuck to the

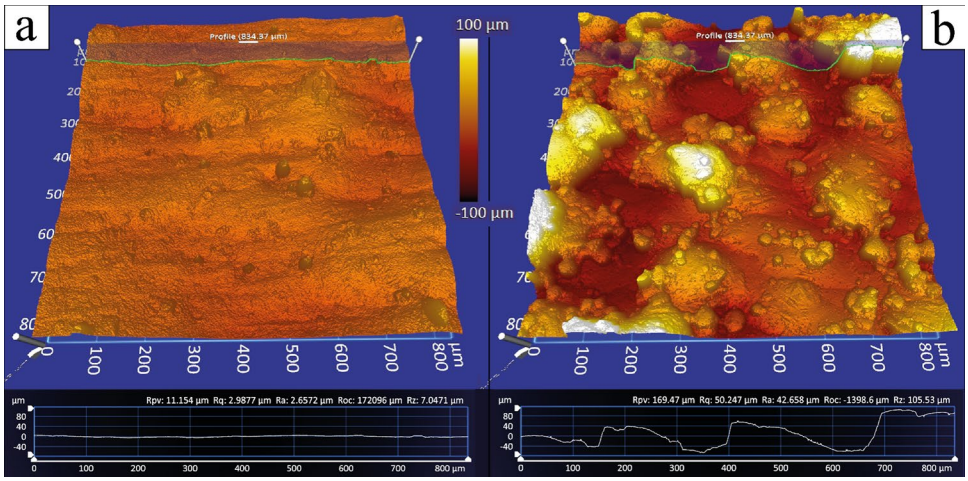

Fig. 6 White-light interferometry images of the surfaces of **a** standard parameter specimen and **b** modified parameter specimen along with a respective roughness profile, highlighting the large differences in surface roughness and irregularities

surface are not considered sites of crack nucleation as long as they extend outward from the part profile [14]. Surface and sub-surface defects such as pores and sharp edges, however, are considered to have a large impact on the fatigue performance of build parts, as they act as crack initiation sites under cyclic loading [14, 23, 24]. Surface finishing techniques such as sandblasting and milling, however, do not consistently eliminate these defects and thus exhibit inconsistent improvements in the fatigue behaviour of PBF–LB specimens [15, 16]. Surface post-processing of cellular structures also proves to be a challenging endeavour due to inaccessible surfaces.

3.2 Porosity

In the micrographs of the samples shown in Fig. 7, it can be observed that the modified parameter samples exhibit significantly fewer pores in the delicate structure region than the standard parameter samples. This is not the case in the shaft, which consists of a larger volume. The optical analysis using ImageJ reveals that the shafts of the modified parameter sample exhibit a relative density of 99.9%, while the shafts of the standard parameter sample are marginally lower at 99.87%. However, when focusing solely on the thin-walled structure area, the difference in relative density is drastic, with 99.90% for the modified parameter sample and only 99.17% for the standard parameter sample. As software was employed to measure the percentage porosity, it is conceivable that the resolution of the images may not permit the consideration of the finest pores present. The optical contrast between the porosities depicted in Fig. 7 appears to be significant, whereas the numerical difference only amounts to a delta of 0.73%.

With a few exceptions, all pores exhibit high sphericity, indicating they consist of entrapped gas. Given that the standard parameter operates with more than double the track energy density (TED) of the modified parameter and a slower scan speed, the material's liquefaction and solidification occur rapidly upon single exposure of the thin wall contour. This could potentially result in the entrapment

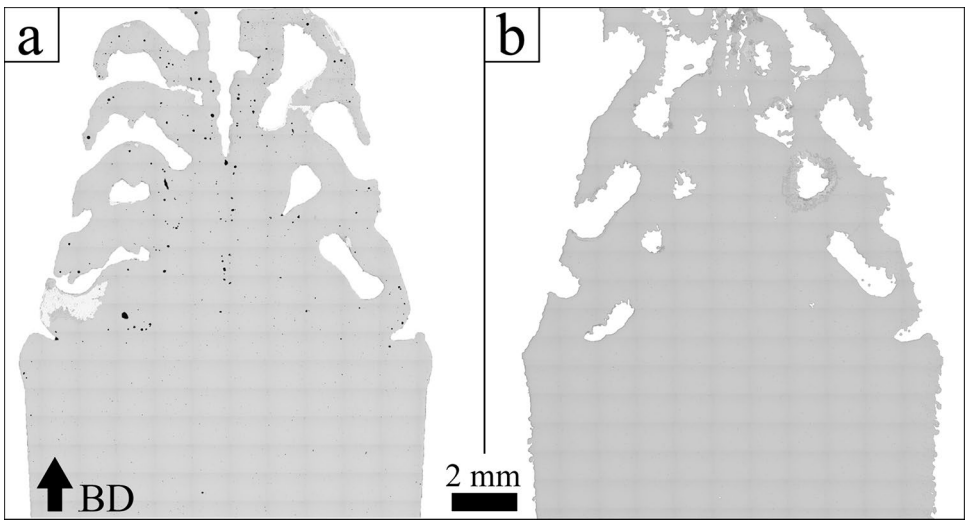

Fig. 7 Light microscope image of micrographs of the thin-walled gyroid structure after rupture of a **a** standard parameter specimen and a **b** modified parameter specimen with the build direction (BD) being up, showing the difference in porosity within the thin-walled structures

of gas formed due to vaporization of material [25, 26], or due to the entrapment of shield gas because of surface turbulence in the melt pool [27]. The large pores in the standard parameters always formed at the centre of a weld track. Aboulkhair et al. [26] also reported increased gas pore formation in AlSi10Mg samples manufactured with slow scanning speeds at high energy densities. Pores have been shown to significantly influence the fatigue behaviour of PBF–LB AlSi10Mg parts, as they can act as internal crack initiation sites [28–30].

3.3 Hardness

The Vickers hardness test results are presented in Fig. 8. The central part of the graph displays the distance of the measuring points from the bottom of the sample, with corresponding hardness values on the left and right for each tested specimen. The fracture point is marked with a dashed line, and the build direction (BD) is indicated by an arrow. Within the shafts, the average hardness for the standard parameter sample is 103.5 ± 3.4 HV0.3, while for the modified parameter sample, it is 99.7 ± 3.6 HV0.3. Regarding the fine structures, the standard parameters yielded a hardness of 84.3 ± 7.9 HV0.3, whereas the modified parameters resulted in a hardness of 94.9 ± 5.9 HV0.3. Published literature reports a range of values between 95 and 135 HV [13, 31–33] for as-built PBF–LB AlSi10Mg, positioning our specimens below the typical hardness of as-built PBF–LB AlSi10Mg. The AlSi10Mg powder from the manufacturer is specified to yield parts with a hardness of 124 ± 7 HV5, while the heat-treated condition is noted at 82 ± 1 HV5 [34]. Reduced hardness has been associated with a coarser microstructure in PBF–LB AlSi10Mg specimens [13, 35], suggesting microstructure coarsening in the specimens manufactured in this work, particularly within the thin wall sections. This effect seems to be more prominent in areas where the low build volume hampers heat dissipation through the build part, leading to slower cooling of the solidified material. A coarsening in microstructure is generally associated with an improved ductility. Another possible factor that can contribute to reduced hardness is the decreased supersaturation of aluminium crystals with silicon particles resulting from a slower cooling rate [36].

The wide range in reported hardness values indicates that both the geometry and process parameters have a significant impact on the resulting hardness. This can be attributed to the resulting thermal profile of the specimen during manufacture, which varies significantly based on energy density, exposure strategy, and available volume for heat dissipation. This variability is known to affect the microstructure and thus influences the hardness [31, 35].

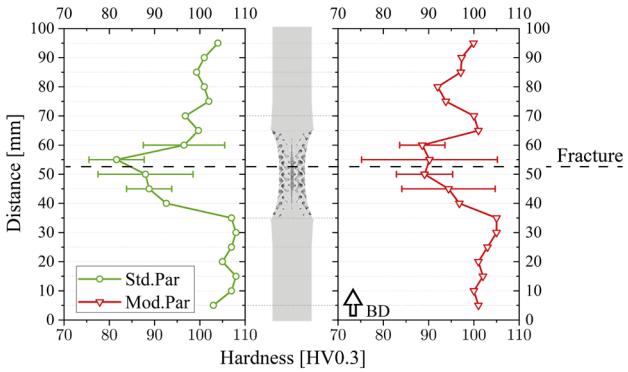

Fig. 8 Hardness measurement comparison of the standard vs. the modified parameter specimens along the rotary axis

3.4 Microstructure

The inhomogeneous microstructure of as-built PBF–LB AlSi10Mg usually consists of cellular α-Al dendrites with ultra-fine eutectic Si networks at their boundaries [17], with the Al dendrites growing epitaxially in the build direction. It is strongly influenced by the melt pool and can be divided into three zones: a fine cellular zone, a coarse cellular zone, and the heat-affected zone in the previously solidified layers [33]. Figure 9 displays comparative SEM images of the standard and modified parameter samples, taken at a random location below the fracture point in the thin-walled structure. Due to the microstructure's division into different regions depending on the melt pool, a quantitative comparison of grain size cannot be provided here. However, it is evident that the eutectic Si network in the modified parameter sample varies significantly at the observed location due to the repeated energy input resulting from the two contours, alternating between a fine cellular structure and a broken, coarser distributed Si phase, as is common for PBF–LB manufactured specimens [13, 33, 37]. In contrast, the SEM image of the sample with standard parameters displays a relatively uniform coarser cellular structure. The decrease in hardness observed in the thin walls of the standard parameters could suggest, that the fast energy input and higher platform temperature linked to these parameters may lead to grain coarsening due to prolonged exposure to elevated temperatures, a phenomenon documented by other researchers [13, 33]. This could potentially lead to a deterioration in mechanical behaviour following the Hall–Petch relationship.

3.5 Fatigue performance

All specimens exhibited consistent fracture behaviour, breaking near the centre of the sample with the fracture point slightly shifted upward in the direction of construction. Since all samples fractured at the same point, a qualitative

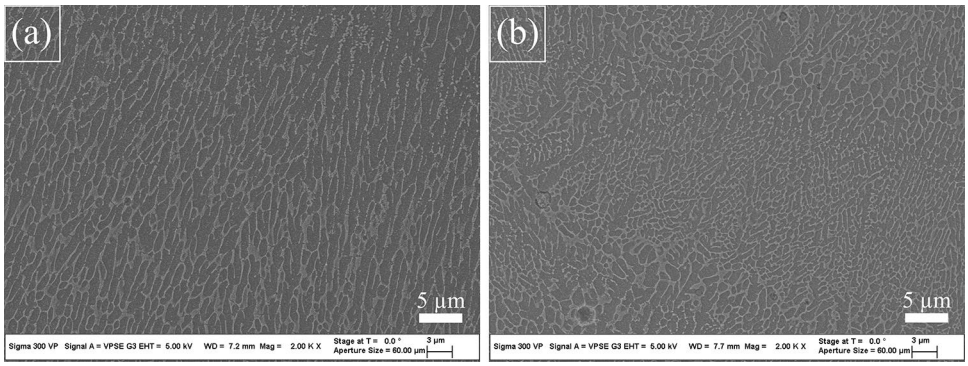

Fig. 9 SEM images of the microstructure in the thin walls of the gyroid structures of a (left) Std.Parameter sample and (right) Mod.Parameter sample

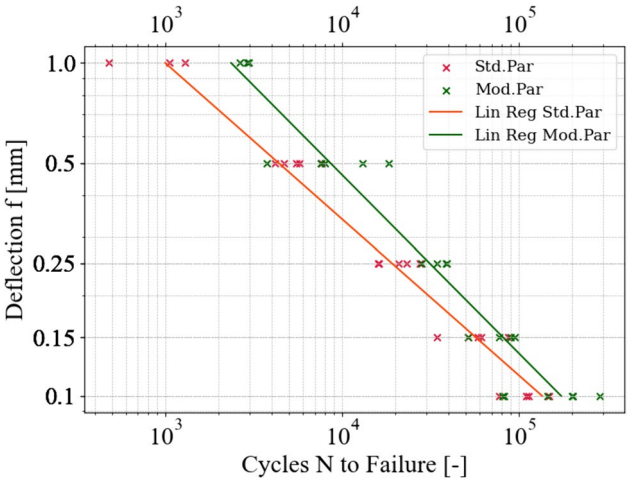

Fig. 10 Woehler line of the standard parameters and the modified parameters with the y axis showing the displacement f instead of the applied stress

comparison can be made. The results of the rotating bending tests for specimens manufactured using AlSi10Mg standard parameters and modified parameters are depicted in Fig. 10. The graph shows the deflection *"f"* at the centre of each sample on the *y*-axis and the corresponding number of cycles until failure on the *x*-axis, both on a logarithmic scale. Linear regressions were calculated for each dataset in accordance with the ASTM E739-23 standard [38], represented by two straight lines with a slope of -0.47 for the standard parameters and -0.54 for the modified parameters. The samples manufactured with the modified parameters exhibit improved fatigue resistance, evident from the rightward shift of the linear regression lines.

As discussed in the respective sections, two mechanisms could be responsible for these effects, both stemming from the reduced track energy density: Firstly, a high TED can lead to grain coarsening due to prolonged exposure to elevated temperatures, consequently diminishing the mechanical properties. Secondly, the high TED seems to contribute to the formation of numerous pores within the thin walls of the standard parameter specimens, negatively impacting their fatigue performance. While surface defects are considered a main contribution factor to the fatigue resistance of additively manufactured (AM) parts [39], in the tested specimens, the influence of build defects and microstructural changes seem to outweigh the impact of poor surface quality. This is evident as the modified parameter samples exhibit significantly improved performance in the high-cycle fatigue range.

The slightly reduced slope of the linear regression line for the standard parameter samples compared to the modified parameter samples suggests that microstructural effects as well as build defects become more significant at larger deflections. Conversely, this implies that the high surface roughness becomes more pronounced at higher cycle numbers, as the lines converge in the high cycle fatigue region. None of the deflection horizons appear to reach the knee point in the conducted tests, which usually indicates the transition to the endurance limit region, characterized by a wider scatter of results [12]. Beretta et al. [39] indicated that the knee point for PBF–LB as-built AlSi10Mg lies around 4×10^6 cycles in tension fatigue tests of solid samples with similar outer geometry, yet complexities in our structure might reduce fatigue strength.

4 Conclusion

Two sets of specimens, composed of triply periodic minimal surface gyroid unit cells, were manufactured using the AlSi10Mg standard parameters and a modified parameter set. These specimens were subjected to rotating bending tests to assess their fatigue behaviour. Additionally, the study encompassed evaluations of surface roughness, optical porosity, hardness, and microstructure and the results were discussed.

In conclusion, the observed change in surface roughness, porosity, hardness, and microstructure among the specimens can be attributed to the reduced track energy density resulting from the adjustments in border distance and laser power.

Despite a significant 7.3-fold rise in surface roughness, the modified parameter samples demonstrate notably enhanced fatigue behaviour. This improvement can be associated with the substantial reduction of pores in the thin walls of the modified parameter samples, which are known to serve as initiation points for cracks under cyclic loading.

The modification of scan parameters can lead to a reduced frequency of pores and finer grain size in thin-walled structures, resulting in a marked improvement in fatigue strength despite the deterioration in surface roughness. Consequently, as-built TPMS structures subjected to bending stress can be employed if the application does not require stringent surface finish.

The use of rotary bending tests proves to be suitable for evaluating additively manufactured intricate cell structures under cyclic bending stress. If application demands do not necessitate specific surface quality, or if a rough surface is desired, optimizing process parameters can yield a fatigue strength improvement surpassing the gains achieved through surface roughness reduction. This offers an economic consideration as minimizing surface roughness may be impractical or resource-intensive. Hence, keeping the surface as-built and focusing on pore reduction with minimal effort might be a more viable approach.

Acknowledgements This research was supported by the German Federal Ministry of Education and Research within the program "FH-Impuls" (Project SmartPro, Subproject Smart-ADD, Grant no. 13FH4I06IA). We would like to extend our sincere appreciation to our colleague Michael Sedlmajer, M.Eng for his invaluable contributions and support throughout the course of this research.

Funding Open Access funding enabled and organized by Projekt DEAL. This work was funded by Bundesministerium für Bildung und Forschung, 13FH4I06IA

Data availability The authors declare that the data supporting the findings of this study are available within the paper. Should any raw data files be needed in another format they are available from the corresponding author upon reasonable request.

Declarations

Conflict of interest The authors have no financial or proprietary interests in any material discussed in this article.

References

1. Wohlers TT, Campbell I, Diegel O et al (2022) Wohlers report 2022: 3D printing and additive manufacturing global state of the industry. Wohlers Associates, Fort Collins, Colorado
2. McGregor M, Patel S, McLachlin S et al (2021) Architectural bone parameters and the relationship to titanium lattice design for powder bed fusion additive manufacturing. Addit Manuf 47:102273. https://doi.org/10.1016/j.addma.2021.102273
3. Ashby MF, Medalist RFM (1983) The mechanical properties of cellular solids. Metall Trans A 14:1755–1769. https://doi.org/10.1007/BF02645546
4. Maconachie T, Leary M, Lozanovski B et al (2019) SLM lattice structures: properties, performance, applications and challenges. Mater Des 183:108137. https://doi.org/10.1016/j.matdes.2019.108137
5. Zhang L, Feih S, Daynes S et al (2018) Energy absorption characteristics of metallic triply periodic minimal surface sheet structures under compressive loading. Addit Manuf 23:505–515. https://doi.org/10.1016/j.addma.2018.08.007
6. AlQaydi HA, Krishnan K, Oyebanji J et al (2022) Hybridisation of AlSi10Mg lattice structures for engineered mechanical performance. Addit Manuf 57:102935. https://doi.org/10.1016/j.addma.2022.102935
7. Li D, Liao W, Dai N et al (2018) Optimal design and modeling of gyroid-based functionally graded cellular structures for additive manufacturing. Comput Aided Des 104:87–99. https://doi.org/10.1016/j.cad.2018.06.003
8. Mahmoud D, Tandel SRS, Yakout M et al (2023) Enhancement of heat exchanger performance using additive manufacturing of gyroid lattice structures. Int J Adv Manuf Technol 126:4021–4036. https://doi.org/10.1007/s00170-023-11362-9
9. Sun Q, Sun J, Guo K et al (2022) Investigation on mechanical properties and energy absorption capabilities of AlSi10Mg triply periodic minimal surface sheet structures fabricated via selective laser melting. J Materi Eng Perform 31:9110–9121. https://doi.org/10.1007/s11665-022-06883-5
10. Yan C, Hao L, Hussein A et al (2015) Ti-6Al-4V triply periodic minimal surface structures for bone implants fabricated via selective laser melting. J Mech Behav Biomed Mater 51:61–73. https://doi.org/10.1016/j.jmbbm.2015.06.024
11. Bobbert FSL, Lietaert K, Eftekhari AA et al (2017) Additively manufactured metallic porous biomaterials based on minimal surfaces: a unique combination of topological, mechanical, and mass transport properties. Acta Biomater 53:572–584. https://doi.org/10.1016/j.actbio.2017.02.024
12. Radaj D, Vormwald M (2007) Ermüdungsfestigkeit: Grundlagen für Ingenieure, 3, neubearbeitete und, erweiterte. Springer-Verlag, Berlin Heidelberg, Berlin, Heidelberg
13. Poncelet O, Marteleur M, van der Rest C et al (2021) Critical assessment of the impact of process parameters on vertical roughness and hardness of thin walls of AlSi10Mg processed by laser powder bed fusion. Addit Manuf 38:101801. https://doi.org/10.1016/j.addma.2020.101801
14. Hamidi Nasab M, Giussani A, Gastaldi D et al (2019) Effect of surface and subsurface defects on fatigue behavior of AlSi10Mg alloy processed by laser powder bed fusion (L-PBF). Metals 9:1063. https://doi.org/10.3390/met9101063
15. Mower TM, Long MJ (2016) Mechanical behavior of additive manufactured, powder-bed laser-fused materials. Mater Sci Eng, A 651:198–213. https://doi.org/10.1016/j.msea.2015.10.068
16. Nicoletto G (2020) Influence of rough as-built surfaces on smooth and notched fatigue behavior of L-PBF AlSi10Mg. Addit Manuf 34:101251. https://doi.org/10.1016/j.addma.2020.101251

17. Roveda I, Serrano-Munoz I, Kromm A et al (2022) Investigation of residual stresses and microstructure effects on the fatigue behaviour of a L-PBF AlSi10Mg alloy. Procedia Structural Integrity 38:564–571. https://doi.org/10.1016/j.prostr.2022.03.057
18. Riva L, Ginestra PS, Ceretti E (2021) Mechanical characterization and properties of laser-based powder bed–fused lattice structures: a review. Int J Adv Manuf Technol 113:649–671. https://doi.org/10.1007/s00170-021-06631-4
19. Brenne F, Niendorf T, Maier HJ (2013) Additively manufactured cellular structures: Impact of microstructure and local strains on the monotonic and cyclic behavior under uniaxial and bending load. J Mater Process Technol 213:1558–1564. https://doi.org/10.1016/j.jmatprotec.2013.03.013
20. DIN 50113:2018–12, Prüfung metallischer Werkstoffe- Umlaufbiegeversuch
21. Schoen AH (1970) Infinite periodic minimal surfaces without self-intersections. NASA Technical Note. https://ntrs.nasa.gov/citations/19700020472
22. Schneider CA, Rasband WS, Eliceiri KW (2012) NIH Image to ImageJ: 25 years of image analysis. Nat Methods 9:671–675. https://doi.org/10.1038/nmeth.2089
23. Aboulkhair NT, Maskery I, Tuck C et al (2016) Improving the fatigue behaviour of a selectively laser melted aluminium alloy: influence of heat treatment and surface quality. Mater Des 104:174–182. https://doi.org/10.1016/j.matdes.2016.05.041
24. Beretta S, Romano S (2017) A comparison of fatigue strength sensitivity to defects for materials manufactured by AM or traditional processes. Int J Fatigue 94:178–191. https://doi.org/10.1016/j.ijfatigue.2016.06.020
25. Dai D, Gu D (2015) Effect of metal vaporization behavior on keyhole-mode surface morphology of selective laser melted composites using different protective atmospheres. Appl Surf Sci 355:310–319. https://doi.org/10.1016/j.apsusc.2015.07.044
26. Aboulkhair NT, Everitt NM, Ashcroft I et al (2014) Reducing porosity in AlSi10Mg parts processed by selective laser melting. Addit Manuf 1–4:77–86. https://doi.org/10.1016/j.addma.2014.08.001
27. Olakanmi EO, Cochrane RF, Dalgarno KW (2015) A review on selective laser sintering/melting (SLS/SLM) of aluminium alloy powders: processing, microstructure, and properties. Prog Mater Sci 74:401–477. https://doi.org/10.1016/j.pmatsci.2015.03.002
28. Siddique S, Imran M, Rauer M et al (2015) Computed tomography for characterization of fatigue performance of selective laser melted parts. Mater Des 83:661–669. https://doi.org/10.1016/j.matdes.2015.06.063
29. Kempen K, Thijs L, van Humbeeck J et al (2012) Mechanical properties of AlSi10Mg produced by selective laser melting. Phys Procedia 39:439–446. https://doi.org/10.1016/j.phpro.2012.10.059
30. Beevers E, Brandão AD, Gumpinger J et al (2018) Fatigue properties and material characteristics of additively manufactured AlSi10Mg—Effect of the contour parameter on the microstructure, density, residual stress, roughness and mechanical properties. Int J Fatigue 117:148–162. https://doi.org/10.1016/j.ijfatigue.2018.08.023
31. Awd M, Siddique S, Johannsen J et al (2019) Very high-cycle fatigue properties and microstructural damage mechanisms of selective laser melted AlSi10Mg alloy. Int J Fatigue 124:55–69. https://doi.org/10.1016/j.ijfatigue.2019.02.040
32. Uzan NE, Ramati S, Shneck R et al (2018) On the effect of shot-peening on fatigue resistance of AlSi10Mg specimens fabricated by additive manufacturing using selective laser melting (AM-SLM). Addit Manuf 21:458–464. https://doi.org/10.1016/j.addma.2018.03.030
33. Thijs L, Kempen K, Kruth J-P et al (2013) Fine-structured aluminium products with controllable texture by selective laser melting of pre-alloyed AlSi10Mg powder. Acta Mater 61:1809–1819. https://doi.org/10.1016/j.actamat.2012.11.052
34. SLM Solutions AG (2017) AISi10Mg Aluminium alloy Material datasheet, SLMSolutions Group AG. https://www.slm-solutions.com/fileadmin/Content/Powder/MDS/MDS_Al-Alloy_AlSi10Mg_0221.pdf. Accessed 8 Apr 2024
35. Tang M, Pistorius PC (2017) Anisotropic mechanical behavior of AlSi10Mg parts produced by selective laser melting. JOM 69:516–522. https://doi.org/10.1007/s11837-016-2230-5
36. Liu YJ, Liu Z, Jiang Y et al (2018) Gradient in microstructure and mechanical property of selective laser melted AlSi10Mg. J Alloy Compd 735:1414–1421. https://doi.org/10.1016/j.jallcom.2017.11.020
37. Trevisan F, Calignano F, Lorusso M et al (2017) On the selective laser melting (SLM) of the AlSi10Mg alloy: process, microstructure, and mechanical properties. Materials (Basel). https://doi.org/10.3390/ma10010076
38. E08 Committee ASTM E739–23: Practice for Statistical Analysis of Linear or Linearized Stress-Life (S-N) and Strain-Life (-N) Fatigue Data
39. Beretta S, Patriarca L, Gargourimotlagh M et al (2022) A benchmark activity on the fatigue life assessment of AlSi10Mg components manufactured by L-PBF. Mater Des 218:110713. https://doi.org/10.1016/j.matdes.2022.110713